Delft University of Technology

Feedback-feedforward individual pitch control design for wind turbines with uncertain measurements

Unguran, Robert; Petrovic, Vlaho; Boersma, Sjoerd; Van Wingerden, Jan Willem; Pao, Lucy Y.; Kuhn, Martin

Important note
To cite this publication, please use the final published version (if applicable).
Please check the document version above.

Feedback-feedforward individual pitch control design
for wind turbines with uncertain measurements

Róbert Ungurán[1], Vlaho Petrović[1], Sjoerd Boersma[2], Jan-Willem van Wingerden[2], Lucy Y. Pao[3], Martin Kühn[1]

Abstract— As the diameters of wind turbine rotors increase, the loads across the rotors are becoming more uneven due to inhomogeneous wind fields. Therefore, more advanced passive or active load reduction techniques are introduced to mitigate these uneven loads. Furthermore, measuring the disturbance can help to improve the control performance. This paper first examines how robust stability and performance are affected by uncertain sensor measurements when an integrator-based feedback is extended with an inversion-based feedforward individual pitch controller with similar bandwidth. A fixed-structured $\mathcal{H}_\infty$ feedback-feedforward controller is proposed. The proposed feedback-feedforward controller ensures robust stability and performance and achieves better load reduction than a classical integrator-based feedback controller combined with inversion-based feedforward controller.

I. INTRODUCTION

The ongoing trend of steadily growing rotor diameters of wind turbines is resulting in dynamic loads which are becoming more uneven across the rotor swept area. Due to the so-called rotational sampling or eddy slicing effect, the blade samples the inhomogeneous wind field with frequencies determined by the rotor speed. Hence, the dynamic blade loads are concentrated at the multiples of the rotational frequency, which are called 1P, 2P, 3P,..., nP. Feedback individual pitch controller [1] and trailing edge flap [2] controllers have been developed to mitigate the dynamic blade loads. Lidar-based feedforward individual pitch [3]–[7] and trailing edge flap control [7] for wind turbines have also been introduced, where a lidar provides a measurement of the disturbance. In these studies, deviations of the inflow wind speed from a nominal speed are considered disturbances. This information can then be used by the feedforward controller. It is shown that such a design can improve the performance of the controller, achieving better rotor speed control and lower tower and blade loads [7]–[9]. In many cases, the feedback collective or individual pitch controller is already given, and it is extended with a reduced bandwidth feedforward controller [3]–[7], [10]. The reasons for this are: (1) the feedback controller is already proven in aeroelastic simulations and field tests, hence it is a risk to replace it, (2) in case of lidar failure or low lidar visibility [10] the feedforward controller

can be switched off. However, such a separated control design can have a negative effect on the overall control performance. If the two controllers have a similar bandwidth, the extension of the feedback with feedforward would lead to a higher peak value of the sensitivity function. Such a controller design can lead to lower sensitivity, hence a better disturbance rejection, at frequencies lower than the cross-over frequency, but unavoidably leads to sensitivity increase around the cross-over frequency [11]. System, disturbance model, or measurement uncertainties will influence the peak value of the sensitivity function, which affects the closed-loop stability and performance [12].

Schlipf et al. [10] carried out field tests with feedback-feedforward collective pitch control with mixed results. When the correlation between the lidar measurement and the estimated rotor effective wind speed was low, the feedforward controller was not beneficial. Navalkar et al. [8] analysed the robustness of lidar-based feedback-feedforward control of floating wind turbines. They showed that taking into account lidar measurement and blade pitch output uncertainties during the control development leads to robust performance and stability and a better rotor speed control. The work of Schlipf et al. [10] and Navalkar et al. [8] highlight how important it is to take into account uncertainties during the feedback-feedforward controller design.

The objective of this paper is to investigate how the performance is affected by combining the classical integrator-based individual pitch feedback control with an inverse-based feedforward control with sensor uncertainties, and to redesign the feedback-feedforward controllers as needed to satisfy robust stability and performance constraints.

This paper is organised as follows: In Section II, the lidar-based simulation setup is introduced and the sensitivity function of the feedback-feedforward control is derived, which is used to analyse the controller performance. In Section III, a classical integrator-based feedback and inversion-based feedforward individual pitch controller are introduced. The controller performance is analysed with uncertain measurements and validated in aeroelastic simulation code. Finally, in Section IV, a mixed sensitivity fixed-structured feedback-feedforward controller is proposed, analysed and validated in aeroelastic simulation code, before the conclusions are drawn in Section V.

[1]ForWind – Center for Wind Energy Research, Institute of Physics, University of Oldenburg, Oldenburg, Germany `robert.unguran@uni-oldenburg.de`

[2]Delft Center for Systems and Control, Faculty of Mechanical Engineering, Delft University of Technology, Delft, The Netherlands

[3]Department of Electrical, Computer, and Energy Engineering, University of Colorado, Boulder, USA
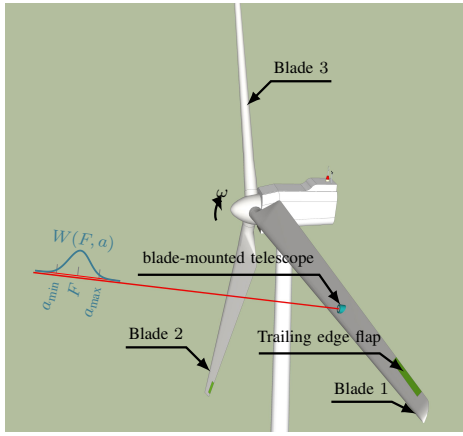
Fig. 1. Lidar measurement configuration, where a telescope is mounted on each blade and is connected through fibre optics to a continuous-wave lidar placed in the hub. The line-of-sight wind speed is computed based on a weighting function ($W(F, a)$) that depends on the focus distance (F) and the range along the beam (a).

II. SIMULATION, ROTOR AND SENSITIVITY FUNCTION DEFINITION

A generic 7.5 MW Type Class Ia wind turbine [13] with a rated wind speed of $10.9 \, \mathrm{m \, s^{-1}}$ and a rated rotor speed of 10 rpm is considered, which was developed within the German Smart Blades project. 10-minute time-domain simulations were carried out for the mean wind speed of $14 \, \mathrm{m \, s^{-1}}$ where the turbulent wind conditions are set in accordance with DLC 1.2 of the IEC 61400-1 ed. 3 standard [14] using the aeroelastic simulation code HAWC2 [15], with the ATEFlap [16] dynamic stall engineering model. Wind shear and tower shadow are also taken into account. 1 Hz damage equivalent loads are calculated, with Wöhler exponents of 3 and 13, which are typical for steel (tower) and composite materials (blade), respectively. The reference controller (REF) is the basic DTU wind energy controller [17], which includes torque and collective pitch control.

A. Rotor and blade-mounted lidar setup

Fig. 1 shows the setup of the investigation. On each 80m m blade, at the span-wise location of 66.4 m, a movable trailing edge flap with a span-wise length of 10 m is introduced. The chord length of the flap is 25 % of the blade chord length, where the flap consists of 5 % flexible and 20 % rigid structure.

On each blade, a telescope is mounted, which is connected to a hub-based continuous-wave lidar with fibre optical cables. The lidar records the inflow wind speed in front of the wind turbine blade at a sampling frequency of 50 Hz. The measurements are used to control the next blade's flap and pitch angle. The blade-mounted lidar simulator is used to model the volumetric measurement and takes into account the dynamics of the blade and tower, i.e., displacement, rotation and velocity in 3D space. The velocity induced by the blade rotation is considered in the lidar simulator as well. The lidar system gives the opportunity for the feedback-feedforward individual pitch control (IPC) and the trailing
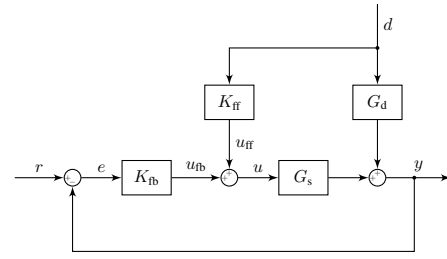

Fig. 2. General block diagram of the feedback-feedforward controller.

edge flap control (TEFC), where the main goal is disturbance rejection. Ungurán and Kühn [18] show an effective feedback IPC and TEFC combination to mitigate the loads occurring once (1P) and twice (2P) per revolution at the flap-wise blade root bending moments. Hence, the objective of the IPC and TEFC are to mitigate the 1P and 2P loads of the flap-wise blade root bending moments, respectively. In this paper, the development of the IPC is elaborated, and the same method is applied during the development of the TEFC.

The above setups are used to test and validate different feedback-feedforward controllers in the sections below.

B. Sensitivity function analysis of feedback-feedforward controller

In this section, the sensitivity function for the feedback-feedforward controller is derived. This enables visually analysing the closed-loop system and identifying e.g., the bandwidth, the peak value of the sensitivity function, and the frequencies where the sensitivity function is above 0 dB. Due to the flexible structure of the wind turbine, knowing these important quantities is critical e.g., the IPC could reduce the blade root bending moments but could excite the tower first natural mode, hence such a design has to be avoided.

For simplicity, a general representation of the feedback-feedforward controller is considered in Fig. 2, where G_s and G_d can be any system and disturbance model, and K_fb and K_ff can be any feedback and feedforward controller. The wind turbine specific implementation is discussed later. The control signal (u) and the output (y) of the system are

$$
\begin{aligned}
u &= K_\mathrm{fb} \left(r - y \right) + K_\mathrm{ff} \, d \\
y &= G_\mathrm{d} \, d + G_\mathrm{s} \, u
\end{aligned}
\tag{1}
$$

For disturbance (d) rejection control design, the reference signal (r) is zero, and the output is thus defined as

$$
y = \left(I + G_\mathrm{s} \, K_\mathrm{fb} \right)^{-1} \left(I + G_\mathrm{s} \, K_\mathrm{ff} \, G_\mathrm{d}^{-1} \right) G_\mathrm{d} \, d
\tag{2}
$$

and the feedback sensitivity (S_fb) and feedforward sensitivity (S_ff) functions are

$$
S_\mathrm{fb} = \left(I + G_\mathrm{s} \, K_\mathrm{fb} \right)^{-1} \quad S_\mathrm{ff} = \left(I + G_\mathrm{s} \, K_\mathrm{ff} \, G_\mathrm{d}^{-1} \right)
\tag{3}
$$

Hence, the sensitivity function for the combined feedback-feedforward controller is defined as

$$
S_\mathrm{fbff} = S_\mathrm{fb} \, S_\mathrm{ff}
\tag{4}
$$

The sensitivity functions in Eqs. (3) and (4) are used to evaluate the controller performances later in this paper. The
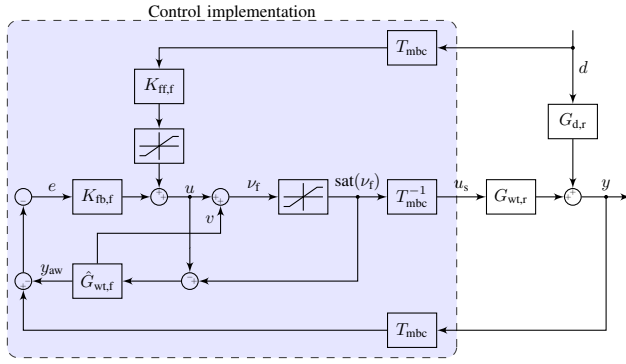
Fig. 3. The general block diagram of the wind turbine feedback-feedforward individual pitch controller implementation, including a model recovery anti-windup filter. Actuator saturation is taken into account in the non-rotating frame of reference. The subscripts r and f refer to the rotating and non-rotating (fixed) frame of references, respectively.

Fig. 4. Singular values of the 2×2 sensitivity functions of the feedback (FB$_I$), feedforward (FF$_I$), and combined feedback-feedforward (FB-FF$_I$) individual pitch controllers. The red dashed and blue dotted constant horizontal lines correspond to $6\,\mathrm{dB}$ and $-3\,\mathrm{dB}$, respectively.

bandwidth of the feedback, feedforward and the combined feedback-feedforward controller is defined where the sensitivity function first crosses the -3 dB line from below.

III. CLASSICAL FEEDBACK-FEEDFORWARD INDIVIDUAL PITCH CONTROLLER

For control development, a simplified wind turbine model is used, which is introduced by Ungurán and Kühn [18]. The model is transformed into the non-rotating frame of reference, applying the multiblade coordinate transformation (MBC) in accordance with Lu et al. [19]. By applying the MBC transformation, the time-variant system with three inputs and three outputs is transformed into a two-input and two-output linear time-invariant system. Fig. 3 shows the control implementation. The individual pitch feedback and feedforward controllers are developed separately. To account for the cross coupling between the yaw and tilt moments, the feedback controller includes the steady-state gains of the inverted wind turbine model ($G_{\mathrm{wt,f}}^{-1}(0)$). To achieve a good disturbance rejection at low frequencies and a good noise rejection at high frequencies the feedback controller is extended with an integrator ($\frac{K_I}{s}$) and a second-order Butterworth low-pass filter ($G_{\ell \mathrm{p}}$). The final form of the integrator-based feedback controller is

$$K_{\mathrm{fb,f}} = G_{\mathrm{wt,f}}^{-1}(0) \, \frac{K_I}{s} \, G_{\ell \mathrm{p}} \; \in \mathbb{C}^{2 \times 2} \tag{5}$$

The starting point of the feedforward control development is an inversion-based feedforward controller. Such a controller would have a high-frequency roll-off, hence only the DC gains of the inversion-based feedforward controller are considered ($-G_{\mathrm{wt,f}}^{-1}(0)\, G_{\mathrm{d,f}}(0)$), and a Butterworth second-order low-pass filter ($G_{\ell \mathrm{p}}$) is added to eliminate actuation at higher frequencies [7]:

$$K_{\mathrm{ff,f}} = -G_{\mathrm{wt,f}}^{-1}(0) \, G_{\mathrm{d,f}}(0) \, G_{\ell \mathrm{p}} \; \in \mathbb{C}^{2 \times 2} \tag{6}$$

The lidar measurements that are taken from blade i are used to evaluate the control signal for pitch angles of the following blade $i - 1$ (see Fig. 1). Therefore, the focus distance and preview time depend on the rotor speed, blade pitch angle
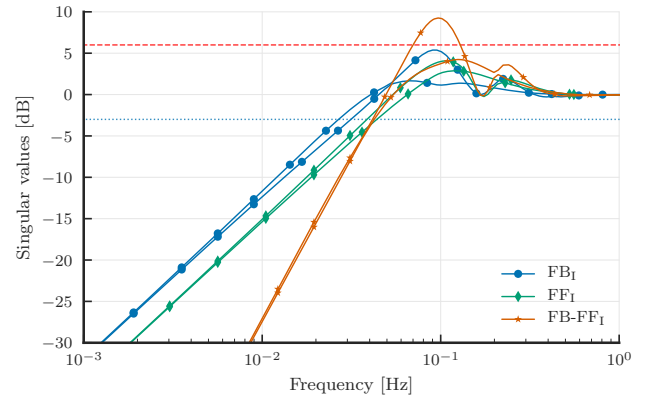
and the mean inflow wind speed. By knowing the operation points of the wind turbine and assuming Taylor's hypothesis [20], the near optimal parameters for $14\,\mathrm{m\,s^{-1}}$ can be found easily. As an example, if the rotation speed around rated wind speed is kept constant at $1.05\,\mathrm{rad\,s^{-1}}$ (10 rpm) and the azimuth angle between two consecutive blades is $2.09\,\mathrm{rad}$ ($120°$), then $2\,\mathrm{s}$ is needed for blade $i - 1$ to reach the azimuth angle of blade i. In reality the wind speed in front of the rotor as well as behind it is retarded due to the rotor induction, which can properly be modelled by Large Eddy Simulations. Here the more common blade element momentum theory is used, where the induction is applied instantaneously only in the rotor plane. Considering the mean pitch angle, the mean hub-height horizontal inflow wind speed, and the rotational speed, this leads to an available preview time of $1.94\,\mathrm{s}$, resulting a focus distance of $27.16\,\mathrm{m}$. Therefore, the second-order Butterworth low-pass filter cut-off frequency is set as $0.12\,\mathrm{Hz}$. This results in a time delay of $1.87\,\mathrm{s}$ [21]. A filter with a lower cut-off frequency would increase the time delay, and hence, the preview time would not be sufficient. Actuator saturation and rate limits are taken into account in the non-rotating frame of reference as proposed in [22]. A model recovery anti-windup filter [7], [23] is included to ensure fast recovery of the feedback controller in case of saturation.

Fig. 4 shows the singular values of the 2×2 sensitivity functions of the feedback (FB$_I$), feedforward (FF$_I$), and combined feedback-feedforward (FB-FF$_I$) individual pitch controllers. The index I refers to the integrator-based feedback and inverse-based feedforward controller. The figure highlights that the sensitivity function of the combined feedback-feedforward controller is increased around the cross-over frequency compared to the feedback control case, which is due to the waterbed effect [12]. It exceeds 6 dB, which is typically not recommended in the literature. A larger value indicates poor performance and may lead to increasing structural loads on the wind turbine components around this frequency. This will later be displayed through aeroelastic simulations.
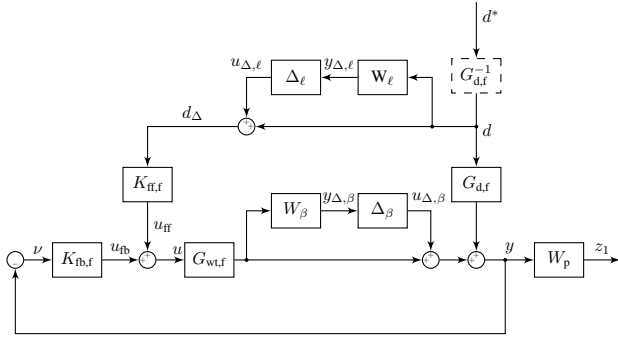
Fig. 5. Block diagram for control design analysis ($d \in \mathbb{R}^2, z_1 \in \mathbb{R}^2, y \in \mathbb{R}^2, u \in \mathbb{R}^2$).

A. Analysis of the closed-loop system with uncertainties

In this investigation the HAWC2 aeroelastic simulation code [15] is used, where wind evolution is considered in accordance with Taylor's frozen hypothesis [20] and the effect of the induction zone is also neglected. These could affect the system stability and performance when it is deployed in field tests. Furthermore, during the estimation of the inflow wind speed from the lidar measurement, perfect measurements of the blade-mounted telescope orientation, blade linear and angular velocities are assumed. However, any sensor misalignment, calibration uncertainty, etc. will lead to over- or underprediction of the inflow wind speed. Uncertainties are also present at the blade root bending moment measurement when strain gauges [24] are used.

In order to analyse the system with uncertainties, Fig. 5 is introduced, which shows how the performance weight ($W_p \in \mathbb{C}^{2 \times 2}$) and uncertainties are considered. Fig. 5 shows that the exogenous output (z_1) is

$$z_1 = W_p \, S_{\text{fbff}} \, G_{\text{d,f}} \, d \tag{7}$$

which highlights that the disturbance model ($G_{\text{d,f}}$) is acting as a scaling of z_1, hence, the inverse of the disturbance model ($G_{\text{d,f}}^{-1}$) is introduced into Fig. 5, shown as a dashed box. This ensures that z_1 is not affected by the disturbance model, so the robust performance and robust stability analysis is a direct indicator of the controller performance in the presence of uncertainties.

For robust performance and stability analysis, diagonal complex uncertainties are considered:

$$\Delta_\ell = \begin{bmatrix} \delta_{\ell,1} & 0 \\ 0 & \delta_{\ell,2} \end{bmatrix}, \quad \Delta_\beta = \begin{bmatrix} \delta_{\beta,1} & 0 \\ 0 & \delta_{\beta,2} \end{bmatrix} \in \mathbb{C}^{2 \times 2}, \tag{8}$$

and $\Delta = \texttt{diag}(\Delta_\ell, \Delta_\beta)$ with property $||\Delta||_\infty \leq 1$, and $\texttt{diag}(\cdot)$ is the diagonal matrix of the elements. The uncertainty weights of the lidar ($W_\ell \in \mathbb{C}^{2 \times 2}$) and blade root bending moment measurement ($W_\beta \in \mathbb{C}^{2 \times 2}$) are defined as first-order minimum-phase shaping filters. They are defined in a way to have a cross-over frequency of 3P (0.5 Hz at rated rotor speed), and represent 20 % uncertainties below 3P ($W_\ell(j0)$) and to reach 300 % at higher frequencies ($W_\ell(j\infty)$). The cross-over frequency is defined where the magnitude of the filter crosses 0 dB from below

($|W_\ell(j\omega_0)| = 1$), which represents 100 % uncertainties. The performance weight is defined to achieve disturbance rejection below 0.01 Hz, leading to a performance weight (W_p^{-1}) which is smaller than 0 dB below this frequency and reaches 10 dB at higher frequencies. The definition of the performance weight requires previous knowledge of the system, e.g., how the system is affected by transforming the 1P frequency from the rotating frame of reference to non-rotating frame of reference by applying the MBC transformation [19].

To assess the influence of the included uncertainties on nominal performance (NP), robust stability (RS), and robust performance (RP), the following generalised plant (P) is obtained

$$\begin{bmatrix} y_{\Delta,\ell} \\ y_{\Delta,\beta} \\ z_1 \\ d_\Delta \\ \nu \end{bmatrix} = \left[\begin{array}{cc|cc} 0 & 0 & W_\ell \, G_{\text{d,f}}^{-1} & 0 \\ 0 & 0 & 0 & W_\beta \, G_{\text{wt,f}} \\ \hline 0 & W_p \, I & W_p \, I & W_p \, G_{\text{wt,f}} \\ I & 0 & G_{\text{d,f}}^{-1} & 0 \\ 0 & -I & -I & -G_{\text{wt,f}} \end{array} \right] \begin{bmatrix} u_{\Delta,\ell} \\ u_{\Delta,\beta} \\ d^* \\ u \end{bmatrix} \tag{9}$$

$$P = \begin{bmatrix} P_{11} & P_{12} & P_{13} \\ P_{21} & P_{22} & P_{23} \\ P_{31} & P_{32} & P_{33} \end{bmatrix} \in \mathbb{C}^{10 \times 8}$$

Assuming nominal stability, RP is ensured when

$$\mu_\Delta(N_i) < 1, \ \forall \omega \quad \text{and} \quad N_i = F_l(P, K_i) \text{ for } i = 1, 2 \tag{10}$$

with $\mu_\Delta(\cdot)$ the structured singular value [25], $F_l(\cdot, \cdot)$ the lower-fractional transformation [12], feedback controller (FB$_I$)

$$K_1 = K_{\text{fb,f}}, \tag{11}$$

combined feedback-feedforward controller (FB-FF$_I$)

$$K_2 = \begin{bmatrix} K_{\text{ff,f}} & K_{\text{fb,f}} \end{bmatrix}, \tag{12}$$

and

$$\begin{bmatrix} y_{\Delta,\ell} \\ y_{\Delta,\beta} \\ z_1 \end{bmatrix} = \underbrace{\begin{bmatrix} N_{i,11} & N_{i,12} \\ N_{i,21} & N_{i,22} \end{bmatrix}}_{N_i} \begin{bmatrix} u_{\Delta,\ell} \\ u_{\Delta,\beta} \\ d^* \end{bmatrix} \tag{13}$$

with dimensions $N_i \in \mathbb{C}^{6 \times 6}$. Assuming nominal stability, RS is ensured when

$$\mu_\Delta(N_{i,11}) < 1, \ \forall \omega \tag{14}$$

and NP when

$$||N_{i,22}||_\infty < 1. \tag{15}$$

The RP, RS and NP tests are done for the closed-loop system with the standalone feedback ($i = 1$, FB$_I$) and combined feedback-feedforward ($i = 2$, FB-FF$_I$) controllers. The results are listed in Table I: while the nominal performance, robust stability, and robust performance are achieved for the feedback case (FB$_I$), robust performance is not achieved when the feedback controller is extended with the feedforward controller (FB-FF$_I$). The robust performance is above 1, which means that the feedback-feedforward IPC does not fulfil the performance requirement in the presence of uncertainties. The following section will illustrate that this can cause undesired behaviour in time-domain simulations.

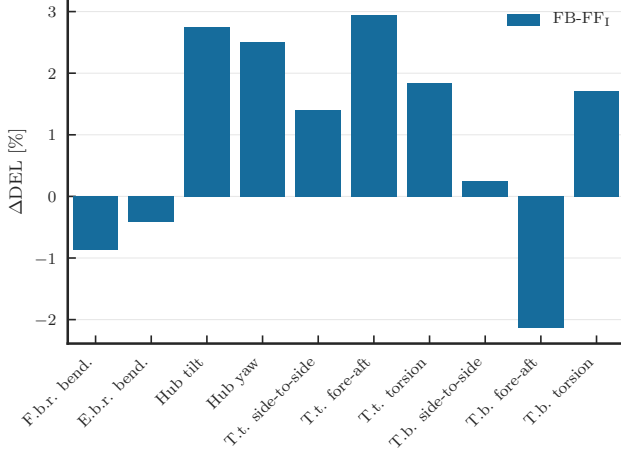|	NP	RS	RP
FB_I	0.20	0.28	0.86
$FB\text{-}FF_I$	0.20	0.28	1.40
$FB\text{-}FF_S$	0.20	0.28	0.98

Fig. 6. The damage equivalent load (DEL) of the combined feedback-feedforward (FB-FF$_I$) IPC case is compared to the feedback (FB$_I$) IPC case. A negative ΔDEL means a DEL reduction of the FB-FF$_I$ controller relative to the FB$_I$ controller. The acronyms of F.b.r and E.b.r. stand for flap-wise and edge-wise blade root. T.t and T.b. stand for tower top and tower bottom.

B. Controller evaluation in aeroelastic simulations

In Fig. 4, it was displayed that the sensitivity function of the combined FB-FF$_I$ IPC is above $6\,\mathrm{dB}$ around the cut-off frequency. This could lead to undesired load increase in this range. Furthermore, the robust performance did not stand for the feedback-feedforward IPC. To assess the controller performance with respect to damage equivalent load reduction, time-domain aeroelastic simulations are carried out. The damage equivalent load reduction (ΔDEL) for several wind turbine components is evaluated according to

$$\Delta\text{DEL} = \left(\frac{\text{DEL}_{\text{FB-FF}_I}}{\text{DEL}_{\text{FB}_I}} - 1 \right) \times 100 \qquad (16)$$

where $\text{DEL}_{\text{FB-FF}_I}$ and DEL_{FB_I} are the 1 Hz damage equivalent load for the FB-FF$_I$ and FB$_I$ IPC, respectively. The relative DEL of FB-FF$_I$ with respect to FB$_I$ IPC is shown in Fig. 6. With the FB-FF$_I$ IPC, a 0.86 % DEL reduction is observed at the flap-wise blade root bending moment. Nonetheless, the DEL of the hub yaw and tilt moments are increased. This has a negative effect at the tower top and bottom loads. The power spectral density of the hub yaw and tilt moments are evaluated and plotted in Fig. 7. The plots show that an additional load reduction, below the $0.04\,\mathrm{Hz}$ cut-off frequency, is achieved by combining integrator-based feedback with inverse-based feedforward controller. However, an undesired peak is observed around 0.1 Hz with the

combined controllers. This is the frequency range where the peak of the sensitivity function can be observed in Fig. 4. This gives motivation to shape the feedback-feedforward controller together, to fulfil the performance requirement and reduce the peak value of the sensitivity function. Therefore, the next section proposes a fixed-structured mixed sensitivity $\mathcal{H}_\infty$ controller.

IV. MIXED SENSITIVITY FIXED-STRUCTURED FEEDBACK-FEEDFORWARD CONTROL

A. Design

To achieve robust stability and performance, a mixed sensitivity control problem without uncertainties is formulated. The block diagram is shown in Fig. 8, where an additional weight ($W_\mathrm{u} \in \mathbb{C}^{2\times2}$) is introduced to penalise the actuator movement. The weight is selected as a high-pass filter with a cross-over frequency of $0.14\,\mathrm{Hz}$. The performance weight (W_p) is equivalent to the one defined in Section III-A. This lead to the new generalised plant (P_f), shown in Eq. (17), which includes the performance and actuator weights, and used for controller synthesising.

$$\begin{bmatrix} z_1 \\ z_2 \\ d \\ \nu \end{bmatrix} = \underbrace{\left[\begin{array}{c|c} W_\mathrm{p}\,I & W_\mathrm{p}\,G_{\mathrm{wt,f}} \\ 0 & W_\mathrm{u}\,I \\ \hline G_{\mathrm{d,f}}^{-1} & 0 \\ -I & -G_{\mathrm{wt,f}} \end{array} \right]}_{P_\mathrm{f}\ \in\ \mathbb{C}^{8\times4}} \begin{bmatrix} d^* \\ u \end{bmatrix} \qquad (17)$$

Next, the cost function is derived. From Eqs. (1) to (3) and (7), the transfer function from the disturbance (d^*) to the controlled output z_1 can be expressed as

$$z_1 = W_\mathrm{p}\,S_{\mathrm{fbff}}\,d^* \qquad (18)$$

The same way, by considering Eqs. (1) and (2), the transfer function from the disturbance (d^*) to the controlled output z_2 can be written as

$$z_2 = W_\mathrm{u}\left(K_{\mathrm{ff,f}}\,G_{\mathrm{d,f}}^{-1} - K_{\mathrm{fb,f}}\,S_{\mathrm{fbff}} \right) d^* \qquad (19)$$

An optimisation problem is formulated, where the goal is to find the feedback ($K_{\mathrm{fb,f}}$) and feedforward ($K_{\mathrm{ff,f}}$) controllers that minimise the following cost function

$$\left\| \begin{bmatrix} W_\mathrm{p}\,S_{\mathrm{fbff}} \\ W_\mathrm{u}\left(K_{\mathrm{ff,f}}\,G_{\mathrm{d,f}}^{-1} - K_{\mathrm{fb,f}}\,S_{\mathrm{fbff}} \right) \end{bmatrix} \right\|_\infty \qquad (20)$$

The fixed-structured controller (FB-FF$_S$) is defined as

$$K_S = \begin{bmatrix} K_{\mathrm{ff,f}} & K_{\mathrm{fb,f}} \end{bmatrix} \qquad (21)$$

with parametrised feedback ($K_{\mathrm{fb,f}}$) and feedforward ($K_{\mathrm{ff,f}}$) controllers from Eqs. (5) and (6). An additional pole (p_{fb}) and zero (z_{fb}) are included in the feedback, and a gain scaling factor (k_{ff}) is included in the feedforward controller to give a higher degree of freedom for the optimiser. This leads to the following representation of the controllers

$$K_{\mathrm{fb,f}} = \underbrace{\left\lfloor G_{\mathrm{wt,f}}^{-1}(0) \right\rfloor}_{2\times2} \frac{k_\mathrm{I}}{s}\,\frac{s - z_{\mathrm{fb}}}{s - p_{\mathrm{fb}}}\,\frac{\omega_{\mathrm{fb}}^2}{s^2 + 2\zeta_{\mathrm{fb}}\omega_{\mathrm{fb}}\,s + \omega_{\mathrm{fb}}^2} \qquad (22)$$
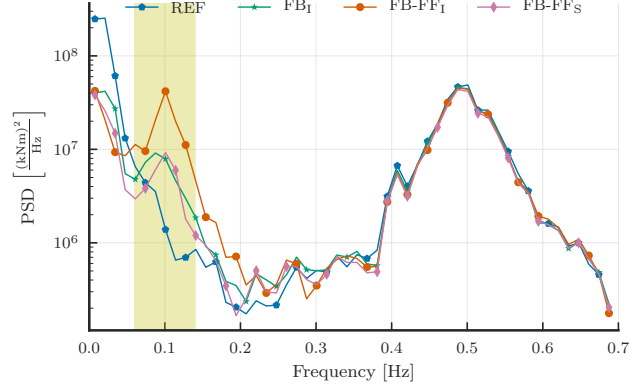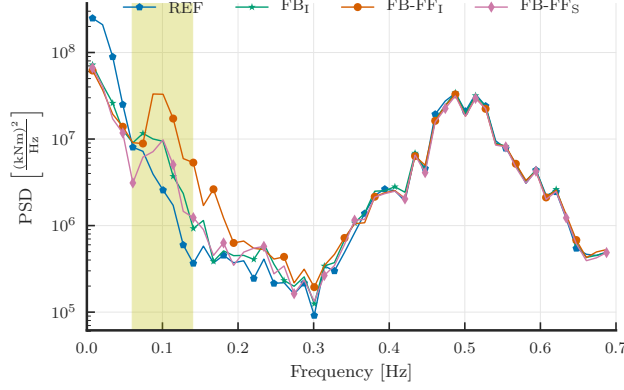
Fig. 7. Power spectral density of the hub yaw (left) and tilt (right) moments. The yellow overlay highlights the range of an induced peak when the feedback is combined with the feedforward controller.
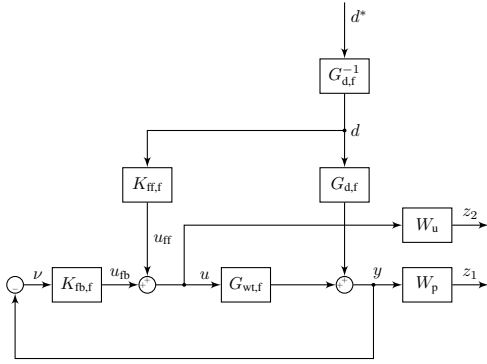

Fig. 8. Block diagram for control design without uncertainties ($d \in \mathbb{R}^2, z_1 \in \mathbb{R}^2, z_2 \in \mathbb{R}^2, y \in \mathbb{R}^2, u \in \mathbb{R}^2$).

Fig. 9. Left: singular values of the 2×2 sensitivity function of the integrator-based (FB-FF$_I$) and the shaped (FB-FF$_S$) feedback-feedforward individual pitch controllers. Right: singular values of the 2×2 sensitivity functions of the shaped feedback (FB$_S$), feedforward (FF$_S$), and combined feedback-feedforward (FB-FF$_S$) individual pitch controllers. The red dashed and blue dotted constant horizontal lines correspond to $6\,\mathrm{dB}$ and $-3\,\mathrm{dB}$, respectively.

$$K_{\mathrm{ff,f}} = \underbrace{\left| -G_{\mathrm{wt,f}}^{-1} G_{\mathrm{d,f}}(0) \right|}_{2 \times 2} k_{\mathrm{ff}} \frac{\omega_{\mathrm{ff}}^2}{s^2 + 2\zeta_{\mathrm{ff}}\omega_{\mathrm{ff}}s + \omega_{\mathrm{ff}}^2} \quad (23)$$

where k_I, z_{fb}, p_{fb}, ζ_{fb}, ω_{fb}, k_{ff}, ω_{ff} and ζ_{ff} are the optimisation variables. In the feedforward controller, a lower bound of the cut-off frequency for the second-order Butterworth low-pass filter is set as $0.12\,\mathrm{Hz}$. A filter with a lower cut-off frequency would increase the time delay, and the preview time provided by the lidar measurement will not be sufficient. For synthesising the fixed-structured controller, the `hinfstruct` function [26] from the robust control toolbox of MATLAB [25] is used.

The left plot of Fig. 9 compares the sensitivity of the integrator-based (FB-FF$_I$) and the shaped (FB-FF$_S$) feedback-feedforward individual pitch controllers. It shows that the performance of the FB-FF$_I$ controller is $40\,\mathrm{dB/decade}$, while for the FB-FF$_S$ controller it is only $20\,\mathrm{dB/decade}$. This leads to a lower peak value of the FB-FF$_S$ controller sensitivity function compared to the one for the FB-FF$_I$ controller. The right plot in Fig. 9 shows the sensitivity functions for the shaped feedback (FB$_S$), feedforward (FF$_S$), and combined feedback-feedforward (FB-FF$_S$) individual pitch controllers. The figure highlights, firstly, that the loop-shaping design results in a lower bandwidth feedback controller compared to the feedforward controller.
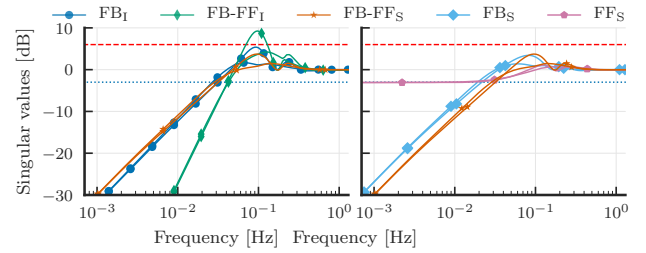
Secondly, that the gains of the FF$_S$ are reduced comparing to the FF$_I$ (see Fig. 4) controller.

To evaluate the performance, the methodology described in Section III-A is applied. The only difference is that the controller is replaced with the fixed-structured mixed sensitivity $\mathcal{H}_\infty$ controller ($N_S = F_l(P, K_S)$). Table I summarises the nominal performance (NP), robust stability (RS), and robust performance (RP) for the three investigated control concepts. The table demonstrates that the FB-FF$_S$ controller fulfils the stability and performance requirements in the presence of sensor measurement uncertainties.

B. Validation

The FB-FF$_S$ controller is evaluated with the HAWC2 aeroelastic simulation code. The power spectral density (PSD) for the hub yaw and tilt moments are shown in Fig. 7. Here, four cases are considered: (1) the reference case (REF), where no load mitigation controllers are active, (2) integrator-based feedback IPC (FB$_I$), (3) integrator-based feedback combined with inversion-based feedforward IPC (FB-FF$_I$), and (4) $\mathcal{H}_\infty$ loop-shaping feedback-feedforward IPC (FB-FF$_S$). The PSD plot shows that with the $\mathcal{H}_\infty$ loop-shaping design the undesired peak at the hub yaw and tilt moments around $0.1\,\mathrm{Hz}$ is reduced. The PSD of the FB-FF$_S$ closely follows the FB$_I$ controller PSD. This is due to, on
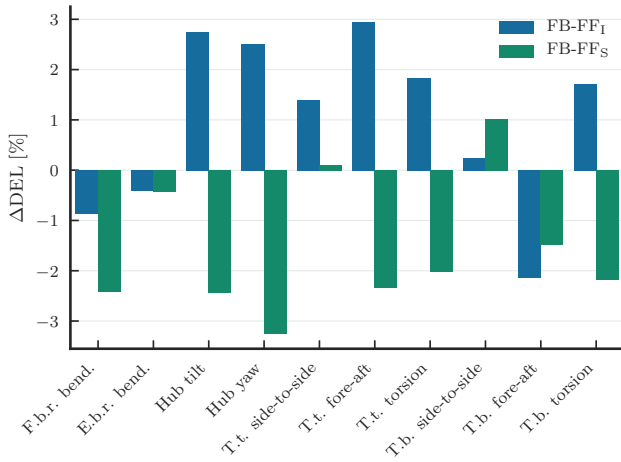
Fig. 10. The damage equivalent load (DEL) of the combined feedback-feedforward (FB-FF$_I$) and $\mathcal{H}_\infty$ loop-shaping feedback-feedforward FB-FF$_S$ individual pitch control is compared to the feedback (FB$_I$) individual pitch control case. A negative DEL means a ΔDEL reduction relative to the FB$_I$ controller. The acronyms F.b.r and E.b.r. stand for flap-wise and edge-wise blade root. T.t. and T.b. stand for tower top and tower bottom.
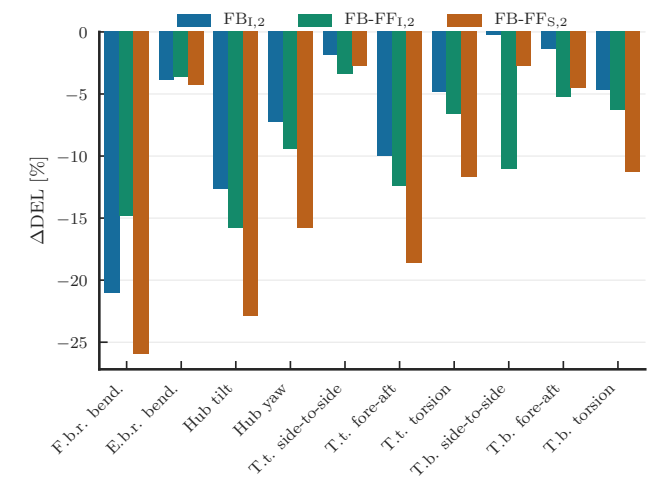

Fig. 11. The damage equivalent load reduction (DEL) of the feedback individual pitch controller (IPC) with trailing edge flap controller (TEFC) (FB$_{I,2}$), the combined feedback-feedforward IPC with TEFC (FB-FF$_{I,2}$) and $\mathcal{H}_\infty$ loop-shaping feedback-feedforward IPC with TEFC (FB-FF$_{S,2}$) compared to the reference case (REF). A negative ΔDEL means DEL reduction relative to the REF case. The acronyms F.b.r and E.b.r. stand for flap-wise and edge-wise blade root. T.t. and T.b. stand for tower top and tower bottom.

the one hand, the cut-off frequencies being similar. On the other hand, below the cut-off frequency the slope of the FB$_I$ and FB-FF$_S$ controller sensitivity function is 20 dB/decade, leading to lower sensitivity deteriorations above the cut-off frequency. The slope of the FB-FF$_I$ controller sensitivity function is 40 dB/decade, leading to higher sensitivity deteriorations above the cut-off frequency due to the Bode sensitivity integral [11], [12].

It should be noted that, due to the reduced feedback control bandwidth, if the lidar system fails and the feedforward is switched off, the FB$_S$ still can be used for load mitigation, but will have a lower performance than the FB$_I$ controller.

The damage equivalent loads (DEL) are evaluated for the FB-FF$_I$ and FB-FF$_S$ IPC cases and compared to the FB$_I$ IPC case, and the results are displayed in Fig. 10. A negative DEL means a ΔDEL reduction relative to the FB$_I$ IPC. The plot highlights that the new control design can further mitigate the loads at the flap-wise blade root bending moment without having negative effects on the hub yaw and tilt moments. The results achieved with the FB-FF$_S$ IPC are expected: The mitigation of the flap-wise blade root bending moment leads to lower hub yaw and tilt moments, which then translate to the tower top and bottom fore-aft and torsion moments. If the results are different, the controller developed for load reduction has to be analysed and redesigned.

To assess the full potential of the smart rotor control with trailing edge flaps and blade-mounted lidars, the individual pitch control (IPC) that is active at 1P is extended with a trailing edge flap controller (TEFC) that is active at 2P. The updated controllers are evaluated in aeroelastic simulations and are compared to the reference case (REF). The damage equivalent load (DEL) reduction for 14 m s^{-1} hub-height mean wind speed is shown in Fig. 11 for the three investigated controller setups: (1) feedback IPC with TEFC (FB$_{I,2}$), (2) combined feedback-feedforward IPC with TEFC (FB-FF$_{I,2}$), and (3) $\mathcal{H}_\infty$ loop-shaping feedback-feedforward IPC with TEFC (FB-FF$_{S,2}$). The plot highlights that extending the feedback controllers with feedforward controllers leads to less blade flapwise and edgewise DEL reduction compared to the FB$_{I,2}$. In general, a better controller performance is expected when the feedback controller is extended with feedforward controller. However, the feedforward controller in FB-FF$_{I,2}$ has a reduced bandwidth to prevent undesired actuation at frequencies higher than 1P for IPC and 2P for TEFC. This results in a higher sensitivity peak around the cross-over frequency of the FB-FF$_{I,2}$ controller case (see Fig. 9), which leads to less DEL reduction compared to the FB$_{I,2}$. This paper shows, that by reducing the peak of the sensitivity function with the proposed $\mathcal{H}_\infty$ loop-shaping feedback-feedforward IPC with TEFC (FB-FF$_{S,2}$), a far superior performance is achieved compared to the integrator-based feedback IPC with TEFC (FB$_{I,2}$).

Furthermore, by extending the feedback IPC with feedforward IPC, a marginal DEL reduction is achieved (see Fig. 10), nevertheless, the feedback-feedforward TEFC improves the DEL reduction significantly. Figs. 10 and 11 underline how beneficial it is to extend the feedback controller with feedforward controller, and that it is mainly useful for the frequencies above 1P.

V. CONCLUSIONS

This paper shows that the stability and performance are affected by measurement uncertainties when a classical integral-based feedback is extended with a reduced bandwidth inversion-based feedforward individual pitch controller (IPC). On the one hand, it is found that robust performance cannot be ensured with the combined integrator-based feedback and reduced bandwith feedforward IPC. On the

other hand, due to the similar cross-over frequencies of the feedback and feedforward IPC, the combined feedback-feedforward IPC sensitivity peak is elevated in comparison to the feedback only case. The controllers are tested in aeroelastic simulation. The results show additional load reduction at the flap-wise blade root bending moment with respect to the feedback only IPC case. However, load increases are observed on the other wind turbine components. These are due to the elevated sensitivity around the cross-over frequency for the combined feedback-feedforward IPC.

This paper highlights the importance of carefully analysing the control performance after combining the feedback with feedforward controller. To achieve the performance objectives, a fixed-structured feedback-feedforward controller is proposed, based on the $\mathcal{H}_\infty$ loop-shaping method. The designed controller achieves robust stability and performance. With the redesigned controller, additional load reductions are achieved across the wind turbine components. The $\mathcal{H}_\infty$ loop-shaping control design results in a reduced bandwidth feedback and an increased bandwidth feedforward controller with respect to the classical integrator-based feedback and inversion-based feedforward controllers. Due to the reduced feedback control bandwidth, if the lidar system fails and the feedforward is switched off, the shaped feedback controller can still be used for load mitigation, but will have a lower performance than the integrator-based feedback controller. Furthermore, the IPC active on 1P is extended with a trailing edge flap controller (TEFC) active on 2P. The extended controller performance is also evaluated in aerolestic simulation code. The proposed controller, based on the $\mathcal{H}_\infty$ loop-shaping method, achieves a better performance with respect to the damage equivalent load reduction across the wind turbine components. This paper points out the importance of reducing the peak value of the combined feedback-feedforward controller sensitivity function around the cross-over frequency to maintain the robust stability and performance, which can easily be achieved with the proposed $\mathcal{H}_\infty$ loop-shaping method.

ACKNOWLEDGEMENT

REFERENCES

[1] E. A. Bossanyi, "Individual blade pitch control for load reduction," *Wind Energy*, vol. 6, no. 2, pp. 119–128, 2003.

[2] J.-W. van Wingerden, A. W. Hulskamp, T. Barlas, B. Marrant, G. A. M. van Kuik, D.-P. Molenaar, and M. Verhaegen, "On the proof of concept of a 'Smart' wind turbine rotor blade for load alleviation," *Wind Energy*, vol. 11, no. 3, pp. 265–280, 2008.

[3] S. Kapp, "Lidar-based reconstruction of wind fields and application for wind turbine control," Ph.D. dissertation, Carl von Ossietzky University of Oldenburg, 2017. [Online]. Available: http://oops.uni-oldenburg.de/3210/1/kaplid17.pdf

[4] D. Schlipf, S. Schuler, P. Grau, F. Allgöwer, and M. Kühn, "Look-ahead cyclic pitch control using lidar," in *The Science of Making Torque from Wind*, 2010.

[5] F. Dunne, D. Schlipf, L. Pao, A. Wright, B. Jonkman, N. Kelley, and E. Simley, "Comparison of two independent Lidar-based pitch control designs," in *50th AIAA Aerospace Sciences Meeting including the New Horizons Forum and Aerospace Exposition*. American Institute of Aeronautics and Astronautics, 2012, pp. 1–19.

[6] E. A. Bossanyi, "Un-freezing the turbulence: application to LiDAR-assisted wind turbine control," *IET Renewable Power Generation*, vol. 7, no. 4, pp. 321–329, 2013.

[7] R. Ungurán, V. Petrović, L. Y. Pao, and M. Kühn, "Performance evaluation of a blade-mounted LiDAR with dynamic versus fixed parameters through feedback-feedforward individual pitch and trailing edge flap control," in *Journal of Physics: Conference Series*, vol. 1037, 2018, p. 032004.

[8] S. Navalkar, J.-W. van Wingerden, P. Fleming, and G. van Kuik, "Integrating robust lidar-based feedforward with feedback control to enhance speed regulation of floating wind turbines," in *American Control Conference*, 2015, pp. 3070–3075.

[9] D. Schlipf, D. J. Schlipf, and M. Kühn, "Nonlinear model predictive control of wind turbines using LIDAR," *Wind Energy*, vol. 16, no. 7, pp. 1107–1129, 2013.

[10] D. Schlipf, P. Fleming, F. Haizmann, A. Scholbrock, M. Hofsäß, A. Wright, and P. W. Cheng, "Field testing of feedforward collective pitch control on the CART2 using a nacelle-based Lidar scanner," in *Journal of Physics: Conference Series*, vol. 555, no. 1, 2014, p. 012090.

[11] G. Stein, "Respect the unstable," *IEEE Control Systems Magazin*, vol. 23, no. 4, pp. 12–25, 2003.

[12] S. Skogestad and I. Postlethwaite, *Multivariable feedback control: Analysis and design, 2nd edition*. John Wiley & Sons, 2005.

[13] J. Teßmer, C. Icpinar, A. Sevinc, E. Daniele, J. Riemenschneider, M. Hölling, C. Balzani, Deutsches Zentrum für Luft- und Raumfahrt, and Deutsches Zentrum für Luft- und Raumfahrt e.V. in der Helmholtz-Gemeinschaft, "Schlussbericht SB: Smart Blades : 01.12.2012-30.04.2016," Tech. Rep., 2016.

[14] International Electrotechnical Commission, *IEC 61400-1 Ed. 3, wind turbines - Part 1: design requirements*, 2005.

[15] T. J. Larsen and A. M. Hansen, "How 2 HAWC2, the user's manual," Tech. Rep., 2007.

[16] L. Bergami, V. A. Riziotis, and M. Gaunaa, "Aerodynamic response of an airfoil section undergoing pitch motion and trailing edge flap deflection: a comparison of simulation methods," *Wind Energy*, vol. 18, no. 7, pp. 1273–1290, 2015.

[17] M. H. Hansen and L. C. Henriksen, *Basic DTU wind energy controller*. Risø, Denmark: DTU Wind Energy, 2013.

[18] R. Ungurán and M. Kühn, "Combined individual pitch and trailing edge flap control for structural load alleviation of wind turbines," in *American Control Conference*, 2016, pp. 2307–2313.

[19] Q. Lu, R. Bowyer, and B. Jones, "Analysis and design of Coleman transform-based individual pitch controllers for wind-turbine load reduction," *Wind Energy*, vol. 18, no. 8, pp. 1451–1468, 2015.

[20] G. I. Taylor, "The spectrum of turbulence," *Proceedings of the Royal Society A: Mathematical, Physical and Engineering Sciences*, vol. 164, no. 919, pp. 476–490, 1938.

[21] F. Dunne and L. Y. Pao, "Optimal blade pitch control with realistic preview wind measurements," *Wind Energy*, vol. 19, no. 12, pp. 2153–2169, 2016.

[22] R. Ungurán, V. Petrović, L. Y. Pao, and M. Kühn, "Smart rotor control of wind turbines under actuator limitations," in *American Control Conference*, 2019.

[23] L. Zaccarian and A. R. Teel, *Modern anti-windup synthesis*, ser. Princeton Series in Applied Mathematics. Princeton University Press, 2011.

[24] K. Papadopoulos, E. Morfiadakis, T. P. Philippidis, and D. J. Lekou, "Assessment of the strain gauge technique for measurement of wind turbine blade loads," *Wind Energy*, vol. 3, no. 1, pp. 35–65, 2000.

[25] G. Balas, R. Chiang, A. Packard, and M. Safonov, *Robust control toolbox – for use with MATLAB*, The Mathworks, Inc., Natick, MA, 2006.

[26] P. Apkarian and D. Noll, "Nonsmooth $\mathcal{H}_\infty$ synthesis," *IEEE Transactions on Automatic Control*, vol. 51, no. 1, pp. 71–86, 2006.